

# A Localizability Constraint-Based Path Planning Method for Autonomous Vehicles

Behnam Irani<sup>ID</sup>, Jingchuan Wang<sup>ID</sup>, and Weidong Chen<sup>ID</sup>, *Member, IEEE*

**Abstract**—During autonomous navigation, environmental information and map noises at different locations may have dissimilar influence on a vehicle’s localization process. This implies that the vehicle’s localizability, i.e., the ability to localize itself in an environment using laser range finder (LRF) readings, varies over a given map. It is essential to take this factor into consideration when planning a path to avoid large localization errors or placing the vehicle at risk of failure to perform localization. We propose a localizability constraint (LC)-based path planning method for autonomous vehicles which plans the navigation path according to LRF sensor model of the vehicle in an effort to maintain a satisfactory level of localizability throughout the path, as well as to reduce the overall localization error. Our method is not limited to any specific algorithm in the optimization stage. Paths planned with and without LC are compared, and the influence of the LRF sensor model on planning outcomes is discussed through simulations. By conducting comparative experiments on a “JiaoLong” intelligent wheelchair in both indoor and outdoor environments, we show that the proposed method effectively lowers the localization error along the planned paths.

**Index Terms**—Autonomous vehicle, path planning, localizability, localization, navigation.

## I. INTRODUCTION

AUTONOMOUS vehicles have continued to attract researchers’ attention over the past few decades due to their potential and significance in human life. In general, autonomous navigation relies on state-of-the-art technologies in perception [1], [2], localization [3], [4], planning [5], [6], and control [7], [8]. Having reliable localization for vehicles throughout planned paths is a basic requirement for many applications in the transportation field. While many GPS-based localization systems have demonstrated great success in outdoor environments, they still suffer in terms of applicability in scenarios with unreliable GPS signals such as indoor or dense urban environments [9], [10]. Laser range finder (LRF) sensor-based localization approaches, due to the accuracy and precision of LRF readings, are still of great importance for both

Manuscript received November 25, 2017; revised June 21, 2018; accepted August 24, 2018. This work was supported by the National Natural Science Foundation of China under Grant 61573243 and Grant 61773261. The Associate Editor for this paper was S. S. Nedevschii. (*Corresponding author: Weidong Chen*)

The authors are with the Key Laboratory of System Control and Information Processing, Ministry of Education of China, Shanghai Jiao Tong University, Shanghai 200240, China, and also with the Shanghai Key Laboratory of Navigation and Location Services, Department of Automation, Shanghai Jiao Tong University, Shanghai 200240, China (e-mail: edmond320@163.com; jchwang@sjtu.edu.cn; wdchen@sjtu.edu.cn).

Color versions of one or more of the figures in this paper are available online at <http://ieeexplore.ieee.org>.

Digital Object Identifier 10.1109/TITS.2018.2868377

indoor and outdoor applications. In this paper, we pay specific attention to global path planning in the presence of localization uncertainty using only LRF as the exteroceptive sensors. During autonomous navigation, environmental information and map noises at different locations may have dissimilar influence on a vehicle’s localization process. This implies that the vehicle’s localizability, i.e., the ability to localize itself in the environment using LRF readings, varies over a given map. In complex and unstructured environments, it is essential to take this factor into consideration when planning a path to avoid large localization errors or placing the vehicle at risk of failure to perform localization. The proposed method is based on the assumption that the environment is known or at least partially known, and that the LRF sensor models are also available, so the response of sensors to the environment can be modeled and simulated.

Primarily, the localization problem can be divided into global localization and pose tracking. Artificial landmarks [11] and multi-sensor based [12] approaches help to deal with the former problem. The goal of pose tracking is to maintain an accurate and rapid tracking of a vehicle’s pose during the whole task, with the initial pose known or given. The most general formulation of path planning under localization uncertainty is selecting optimal action in a partially observable stochastic domain, which is known as Partially Observable Markov Decision Process (POMDP) [13]–[15]. While POMDPs are theoretically satisfactory, they may become computationally intractable as the scale of states grows. Many sampling-based approaches have been extended to deal with such uncertainty, but they typically assume that the belief space is Gaussian, such as the Belief Road Map [16], a variation of the Probabilistic Road Map (PRM) [17]. In [18], generalizations of the PRM and Rapidly-exploring Random Trees (RRT) [19] algorithms were presented to obtain hybrid hierarchical motion planners that are robust to both motion and environmental uncertainty; however, the state of the vehicle is assumed to be perfectly known. Although Extended Kalman Filter [20] and Particle Filter [21] based algorithms perform well in pose tracking, it can still be challenging while vehicles navigate in texture-poor, similarly-featured or noisy regions in the map. In these cases, localization uncertainty increases drastically due to the lack of sufficient valid LRF readings or mismatching, therefore resulting in large localization error.

To tackle this issue, we propose a localizability constraint (LC) based path planning method for autonomous vehicles which explicitly quantifies the influence caused by the

environment on a vehicle's localization process over a prior map before incorporating it into path planning. To solve a multi-objective optimization problem, a common approach is to optimize one primary cost while treating the others as constraints (secondary costs) [22]. In this article, we adopt path length as the primary cost and localizability measure (will be explained in Section II) as constraints. The proposed method determines passable regions on a PGM according to the LRF sensor model and plans paths within this region, thereby promising a satisfactory level of localizability for the vehicle throughout the path. Paths planned with and without LC are compared, and the influence of LRF sensor model on planning outcomes is discussed through simulations. By conducting experiments on a "JiaoLong" intelligent wheelchair [23] in both indoor and outdoor environments, we show that the proposed method effectively reduces the localization error while the wheelchair navigates along the paths.

The remaining of this paper is organized as follows: Section II covers a range of related work including the adopted localizability estimation method. Section III describes the LC-based path planning method. In Section IV, a comparison between paths with and without LC is made via simulation, and the influence of LRF scan models on planning outcomes is discussed. Finally, real world experiments are conducted, and their localization performance is compared in Section V.

## II. RELATED WORK

One way to obtain good localization performance is computing the influence caused by the environment on a vehicle's localization process over a prior map and incorporating it into path planning. To quantify such influence, the attempted approaches are mainly classified into two categories: grid based [24], [25] and geometric map based [26]–[28]. Reference [24] has proposed an entropy-based localizability estimation approach which evaluates the information content at every candidate position. However, entropy is a one-dimensional index that only presents the overall performance of localization and shows no sign of directional properties. Reference [25] has introduced a cross entropy-based method to assess the influence of observation on localization, but its analytical solution is not provided. References [26] and [27] have obtained Fisher's Information Matrix (FIM) using the expected LRF readings and the slope of scanned environmental surfaces in a geometric map, but the influence caused by uncertainty of the map [29] has been neglected. In addition, analytical expression of a map structure is usually not easy to obtain. Reference [28] proposed a concept named "perceptual ambiguity" for sonar sensors, but likewise, it is also based on a geometric map and is not easily applicable as explained.

Some other efforts [30]–[32] tried to minimize the localization uncertainty of the agent at the goal point, but similar to [24], they all assume the scanning system to be *omni-directional* (with an field of view of 360°), which limits their application to other types of sensor models.

Inspired by the results from [26] and [27], and having considered the influence caused by environmental information and map noises on localization at different locations, probabilistic

grid map (PGM) based localizability estimation matrices were introduced in our earlier study [33], namely Static Localizability Matrix (SLM) and Dynamic Localizability Matrix (DLM). These matrices describe the measure and directional properties of localizability in a quantitative manner without extracting any specific observation features, and present the lower-bound of attainable covariance of localization as they were derived using the Cramér-Rao Bound theory [34]. SLM is used to estimate the static localizability over a PGM based on a given LRF sensor model. In DLM, additional attention is paid to the influence of dynamic obstacles on localization, and it indicates the real-time localization performance of the vehicle. In our previous work, SLM and DLM-based methods were studied in applications such as localization in highly-occluded and dynamic environments [35], active global localization [36], and have all been proven to be effective and promising. In this work, we incorporate SLM into global path planning to generate more reliable paths and achieve better localization performance for autonomous vehicles. We introduce localizability estimation approach via SLM as follows.

### A. Static Localizability Matrix

The PGM-based SLM proposed in [33] is obtained by discretizing FIM, which can reflect a vehicle's localizability for any desired pose  $\mathbf{p}$  in a 2-dimentional PGM. For the sake of simplicity, it is considered that the LRF shares the same coordinates with the vehicle which it is equipped on, and the pose of LRF in the PGM frame is given as  $\mathbf{p}_l = [x, y, \theta_l]$ . Given the sensor model, a total of  $N_l$  evenly spaced scan rays may be generated by following the scan sequence of the LRF. The discretized FIM is written as

$$\hat{\mathbf{L}}(\mathbf{p}) = \sum_{i=1}^{N_l} \frac{1}{\sigma_i^2} \left( \frac{\Delta r_{iE}}{\Delta \mathbf{p}} \right)^T \left( \frac{\Delta r_{iE}}{\Delta \mathbf{p}} \right) \quad (1)$$

where

$$\frac{\Delta r_{iE}}{\Delta \mathbf{p}} = \begin{bmatrix} \frac{\Delta r_{iE}}{\Delta x} & \frac{\Delta r_{iE}}{\Delta y} & \frac{\Delta r_{iE}}{\Delta \theta} \end{bmatrix}. \quad (2)$$

$\sigma_i^2$  is the variance of th  $i$ -th LRF scan ray,  $r_{iE}$  is the expected distance to the nearest obstacle of the  $i$ -th LRF scan ray and it is computed based on the known PGM.  $r_{iE}$  is calculated using

$$r_{iE} = \frac{\sum_{j=1}^s r_{ij} \mu_{ij}}{\sum_{j=1}^s \mu_{ij}} \quad (3)$$

where  $r_{ij}$  is the distance between the vehicle's position and  $j$ -th grid along the direction of  $i$ -th LRF scan ray.  $\mu_{ij}$  is the occupancy probability of the corresponding grid, and  $s$  is the sequence number of the ending grid. A grid is considered unoccupied if its occupancy probability is less than a threshold  $T_s$ . Since attention is only paid to the nearest obstacle,  $s$  should meet two conditions:  $\mu_{is} < T_s$  and  $\mu_{i(s-1)} > \mu_{is}$ .

By combining (2) with (1) and substituting  $\mathbf{p}_l$  we obtain

$$\hat{\mathbf{L}}(\mathbf{p}_l) = \sum_{i=1}^{N_l} \frac{1}{\sigma_i^2} \begin{bmatrix} \frac{\Delta r_{iE}^2}{\Delta x^2} & \frac{\Delta r_{iE}^2}{\Delta x \Delta y} & \frac{\Delta r_{iE}^2}{\Delta x \Delta \theta_l} \\ \frac{\Delta r_{iE}^2}{\Delta x \Delta y} & \frac{\Delta r_{iE}^2}{\Delta y^2} & \frac{\Delta r_{iE}^2}{\Delta y \Delta \theta_l} \\ \frac{\Delta r_{iE}^2}{\Delta x \Delta \theta_l} & \frac{\Delta r_{iE}^2}{\Delta y \Delta \theta_l} & \frac{\Delta r_{iE}^2}{\Delta \theta_l^2} \end{bmatrix}. \quad (4)$$

The field of view (FOV) of LRF is noted as  $\Theta_l$ , if it is less than  $360^\circ$ , the SLM of a given position is *orientation-dependent* and needs to be computed separately for every desired orientation. If an omni-directional scanning system is constructed (for example using two or more LRFs), i.e.  $\Theta_l = 360^\circ$ , then the component  $\theta_l$  in the above equation can be omitted, which results in

$$\hat{\mathbf{L}}(\mathbf{p}_l) = \sum_{i=1}^{N_l} \frac{1}{\sigma_i^2} \begin{bmatrix} \frac{\Delta r_{iE}^2}{\Delta x^2} & \frac{\Delta r_{iE}^2}{\Delta x \Delta y} \\ \frac{\Delta r_{iE}^2}{\Delta x \Delta y} & \frac{\Delta r_{iE}^2}{\Delta y^2} \end{bmatrix}. \quad (5)$$

### B. Localizability Measure

According to the Cramér-Rao Bound theory, the localization covariance matrix can be estimated using information matrix, which is SLM in this context:

$$\text{cov}(\mathbf{p}) = \hat{\mathbf{L}}^{-1}(\mathbf{p}). \quad (6)$$

The covariance ellipse can be derived from (6) [37], and its area demonstrates the global achievable accuracy [38]. A smaller area stands for a higher localization accuracy. For example, the covariance ellipse on x-y plane can be derived from  $\hat{\mathbf{L}}_{xy}^{-1}(\mathbf{p})$  which is  $\hat{\mathbf{L}}^{-1}(\mathbf{p})$  with elements containing only  $x$  and  $y$ . Its semi-major axis and semi-minor axis are  $E_{xy}$  and  $F_{xy}$ . Notice that the area of this covariance ellipse is proportional to the eigenvalues of  $\hat{\mathbf{L}}_{xy}^{-1}(\mathbf{p})$  which are  $\lambda_x^{-1}$  and  $\lambda_y^{-1}$ :

$$\pi E_{xy} F_{xy} \propto \lambda_x^{-1} \lambda_y^{-1} = (\lambda_x \lambda_y)^{-1} \equiv [\det(\hat{\mathbf{L}}_{xy}(\mathbf{p}))]^{-1}. \quad (7)$$

Similar results can be concluded on x- $\theta$  and y- $\theta$  planes. To evaluate and compare the expected localization quality of poses over the PGM, the determinant of the SLM is adopted as the measure [33] and is referred to as *localizability measure*  $l(\mathbf{p})$  (LM):

$$l(\mathbf{p}) = \det(\hat{\mathbf{L}}(\mathbf{p})) \equiv \begin{cases} \lambda_x \lambda_y \lambda_\theta, & \text{if } \Theta_l < 360^\circ \\ \lambda_x \lambda_y, & \text{if } \Theta_l = 360^\circ. \end{cases} \quad (8)$$

$l(\mathbf{p})$  is an index that reflects how discriminative the LRF observation at pose  $\mathbf{p}$  is for determining the vehicle's pose in the PGM. A larger  $l(\mathbf{p})$  implies smaller area of covariance ellipse and higher observation information for localization. After calculating the LM of grids over a PGM, a corresponding LM graph is generated. Fig.1(a) is an example environment, Fig.1(b) is the corresponding PGM generated using Gmapping

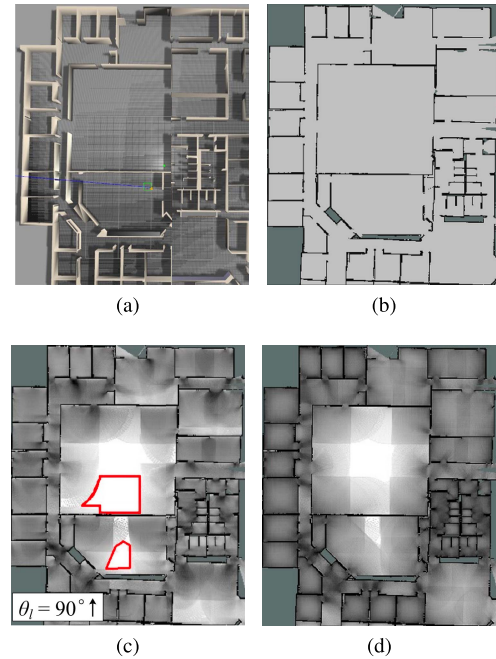


Fig. 1. LM graph illustration and comparison. (a) Example environment. (b) PGM. (c)  $\Theta_l = 180^\circ$ . (d)  $\Theta_l = 360^\circ$ .

SLAM method [39], Fig.1(c) and (d) demonstrate the calculated results in case of  $\Theta_l = 180^\circ$  (with  $\theta_l = 90^\circ$ ) and  $\Theta_l = 360^\circ$  respectively. Whiter grids indicate lesser environmental information, whereas darker grids represent richer information and better localizability when the vehicle is located at those poses or positions (depending on  $\Theta_l$ ). The darkest areas (colored black) are obstacles present in the environment. As can be seen from the figures, richer information is perceived in case of  $\Theta_l = 360^\circ$ . In Fig.1(c), areas marked with red outlines provide absolutely zero information about the environment, whereas in Fig.1(d) the same areas do provide some information due to a larger  $\Theta_l$ . As  $\hat{\mathbf{L}}(\mathbf{p})$  is orientation-dependent with  $\Theta_l < 360^\circ$ , in this case,  $l(\mathbf{p})$  is also orientation-dependent.

## III. LOCALIZABILITY CONSTRAINT BASED PATH PLANNING

### A. Objective Function

Let  $p'$  be an arbitrary path in a PGM which consists of a series of adjacent points  $p$  such that  $p' = \{p_1, p_2, \dots, p_n\}$  where  $n$  is the number of points in the path.  $Dis(p_k, p_{k+1})$  is defined as Euclidean distance between points  $p_k$  and  $p_{k+1}$ , and  $C(p')$  is defined as cost function of path  $p'$ :

$$C(p') = \sum_{k=1}^{n-1} Dis(p_k, p_{k+1}). \quad (9)$$

To obtain the shortest path  $p'_s$  which links the start point  $p_{st}$  and the goal point  $p_{gl}$ , it is sufficient to calculate the solution  $p'$  that meets the following objective function:

$$p'_s = \arg \min_{p'} C(p'), \quad (10)$$

TABLE I  
DEFINITION OF SYMBOLS

Symbol	Definition
$\Theta_l$	Field of view. The field of view of LRF systems equipped on the vehicle. It has a upper limit of $360^\circ$ .
$\phi$	Angular interval. The angular interval used to divide orientations in case of $\Theta_l < 360^\circ$ .
M	Total number of orientations. In case of $\Theta_l = 360^\circ$ , M = 1. In case of $\Theta_l < 360^\circ$ , $M = 360^\circ/\phi$ . For example, $M = 8$ if $\phi = 45^\circ$ .
$m$	a variable that ranges from 1 to M. $m$ -th orientation represents angle $(m - 1) \times \phi$ .
$p_m$	a pose with coordinates of corresponding point $p$ and $m$ -th orientation.
$l'(\mathbf{p})$	Normalized $l(\mathbf{p})$ calculated at pose $\mathbf{p}$ .
$T_{\text{bin}}$	Binarization threshold. Used to filter out grids with low $l'(\mathbf{p})$ .
$T_{\text{incl}}$	Inclusion threshold. Used to include regions with small areas into $\mathbf{R}_{\text{pass}_m}$ .
$\mathbf{R}_{\text{incl}_m}$	Local included region under $m$ -th orientation. A set of points included into $\mathbf{R}_{\text{pass}_m}$ .
$\mathbf{R}_{\text{pass}_m}$	Local passable region under $m$ -th orientation. The passable region in the PGM for vehicle under $m$ -th orientation. It is the union set of points with $l'(\mathbf{p}_m) > T_{\text{bin}}$ and $\mathbf{R}_{\text{incl}_m}$ .
$\mathbf{R}_{\text{pass}}$	Global passable region. The final passable region in the PGM for vehicle. It is the union set of $\mathbf{R}_{\text{pass}_m}$ under orientations 1 to M. Feasible paths are planned within this region in subsequent step.
$\theta_l$	Observing orientation of LRF.
$\theta_r$	Moving direction of the vehicle.
$\varphi$	Angle between $\theta_l$ and $\theta_r$ .
$D_l$	Scan distance. Maximum scan distance of LRF systems equipped on the vehicle.
$R_l$	Scan resolution. Scan resolution of LRF systems equipped on the vehicle.
$N_l$	Number of scan rays. The total number of scan rays of LRF systems equipped on the vehicle.

### B. Constraints

In the proposed method,  $p'_s$  is found on the premise of constraining planning configuration space using the vehicle's LM graph(s):

$$\text{s.t. } \begin{cases} p_k \in \mathbf{R}_{\text{pass}}, \forall p_k \in p'_s \\ \mathbf{R}_{\text{pass}} = \mathbf{R}_{\text{pass}_1} \cup \dots \cup \mathbf{R}_{\text{pass}_M} \\ \mathbf{R}_{\text{pass}_m} = \{p | l'(\mathbf{p}_m) > T_{\text{bin}}\} \cup \mathbf{R}_{\text{incl}_m} \\ m = 1, \dots, M. \end{cases} \quad (11)$$

Definition of symbols is listed in Table I. By posing this constraint, we ensure that most of the points of  $p'_s$  possess desirable  $l'(\mathbf{p})$  and are all within global passable region  $\mathbf{R}_{\text{pass}}$  (refer to Table I). We will show in the following sections that planning a path under such constraint noticeably reduces the overall localization error of the vehicles.

### C. Extraction of Local and Global Passable Regions

To derive  $\mathbf{R}_{\text{pass}}$  in (11), the LM graph(s) and corresponding  $\mathbf{R}_{\text{pass}_m}$  under orientations 1 to M need to be obtained at the outset. The extraction process of  $\mathbf{R}_{\text{pass}_m}$  and  $\mathbf{R}_{\text{pass}}$  is illustrated in Fig.2, and explained in details as follows:

1) *PGM Generation*: Firstly, method such as Gmapping SLAM is used to generate the PGM of the environment in which the vehicle is going to navigate.

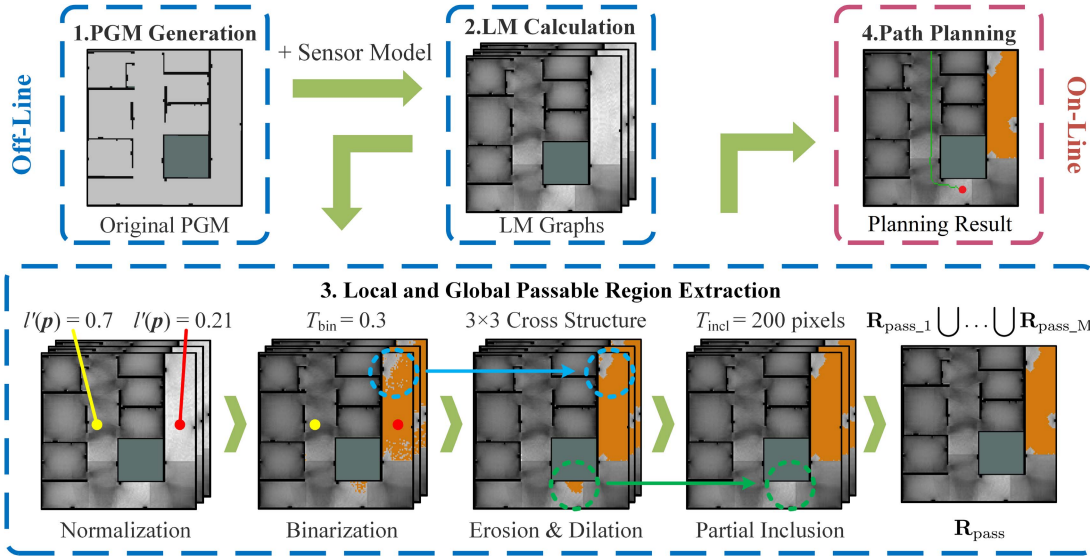
2) *LM Calculation*: In this step,  $l(\mathbf{p})$  over the generated PGM is calculated to produce an LM graph(s). This is done by applying the method provided in Section II, with a specific sensor model taken into consideration. The sensor model specifies  $\Theta_l$ ,  $D_l$ ,  $R_l$  and  $N_l$  listed in Table I. If  $\Theta_l = 360^\circ$  and  $M = 1$ , (5) is used for calculation and only one LM graph is generated. Otherwise (4) is used and a total of M LM graphs are generated.

3) *Normalization*: There may appear a noticeable difference between  $l(\mathbf{p})$ s calculated from distinct environments or from a single environment but using dissimilar sensor models, both in terms of numerical value and order of magnitude. Therefore, a normalization process is required for further processing. One way to do so is using Min-Max normalization method over  $l(\mathbf{p})$ s to produced normalized results  $l'(\mathbf{p})$ s. Values of  $l'(\mathbf{p})$ s are ranged from 0 to 1 with those closer to 1 implying higher and those closer to 0 implying lower localizability.

4) *Binarization*: We wish to filter out grids with low LM (colored orange in the corresponding subgraph) in the LM graphs, this can be done through binarizing  $l'(\mathbf{p})$ s using a threshold  $T_{\text{bin}}$ .  $T_{\text{bin}}$  is determined per specific circumstances by the user: a lower value represents a more conservative filtering strategy and retains more grids from the original PGM, whereas higher value filters the grids in a more radical manner and higher priority is given to localizability of the paths to be planned.

5) *Erosion and Dilation*: Due to the discrete characteristic of the PGM, grids filtered out after binarization are also in discrete form. To ensure that the vehicle does not cross over or unintentionally enter these grids, isolated grids need to be eliminated to generate complete connected regions. We borrow the erosion and dilation operations from Digital Image Processing with structure element  $SE$  and apply them to grids filtered out in the last step to deal with this issue. After these two operations, one or multiple connected regions with low LM would be generated (colored orange in the corresponding subgraph). By subtracting the union set of these regions and obstacle regions from the original PGM, the major part of  $\mathbf{R}_{\text{pass}_m}$  is obtained.

6) *Partial Inclusion*: If a vehicle enters the connected regions with a low LM generated in the previous step, theoretically, its localizability would decrease. However, when it comes to actual performance, it can be carefully assumed that such behavior would not drastically affect its subsequent localization, provided that it only stays in those regions with low LM for a short period of time. Under this premise, we may include some of these regions based on certain criteria to potentially shorten the length of paths to be planned. Considering that the larger area a region possesses, the higher the possibility that a vehicle might be staying in it for a longer period of time, and furthermore, given the fact that majority of the connected regions are of irregular shapes, area of the regions is chosen for inclusion. Those regions that have a smaller area than a given threshold  $T_{\text{incl}}$  form  $\mathbf{R}_{\text{incl}_m}$  and are included into  $\mathbf{R}_{\text{pass}_m}$ . In practice,  $T_{\text{incl}}$  may be determined

Fig. 2. Procedure of the proposed path planning method ( $M = 3$  is shown).

per the accuracy of odometer equipped on the vehicle: a lower accuracy demands a lower threshold and vice versa. At the current stage  $T_{incl}$  is determined empirically, further investigation is required on the relation between these two factors.

**7)  $R_{pass}$  Extraction:** After above steps, in the case of  $M = 1$ ,  $R_{pass}$  is exactly the final extracted  $R_{pass\_1}$ . In other cases,  $R_{pass}$  is generated by extracting  $R_{pass\_1}$  to  $R_{pass\_M}$  and finding their union set, as noted in (11).

#### D. Optimization Method

General concepts of the optimization method used in the proposed framework are explained as follows:

1) Finding  $p'_s$  in (10) is not limited to any specific path planning algorithm. It can be done by implementing algorithms such as A\* [40], RRT and their variations.

2) The parameters  $\phi$  and  $M$  needed to derive  $R_{pass}$  are determined based on the sensor model and actual need of the adopted algorithm. For example, in cases where  $\Theta_1 < 360^\circ$ , as typical A\* algorithms only explore eight adjacent points of the current *expanding point* in each iteration,  $M$  may be set to eight (and therefore  $\phi = 45^\circ$ ). In typical RRT algorithms, since the newly sampled *candidate point* in every iteration may occur at a random orientation of its *nearest existing point* in the tree, theoretically  $\phi$  should be set to  $\theta_l$  to obtain the most accurate LM graphs for every orientation. In fact, the number of  $M$  could be reduced without trading off much accuracy by combining angles within a certain range and using one LM to approximate LMs under these combined angles. In Fig.3, the LM under  $\theta_l$  is calculated to approximate the LMs under orientations between  $\theta_l - \phi/2$  and  $\theta_l + \phi/2$ . As can be easily realized, the maximum angular error of such an approximation is equal to  $\phi/2$ .

3) To solve for  $p'_s$ , a potential modification is made to incorporate LC into path planning algorithms. By examining  $\Theta_1$  and  $\phi$  (see Table I), path planning is performed in three slightly different ways:

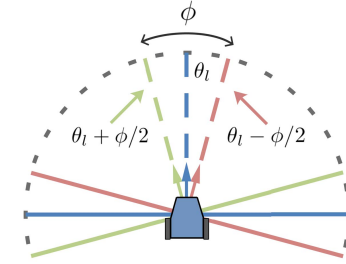
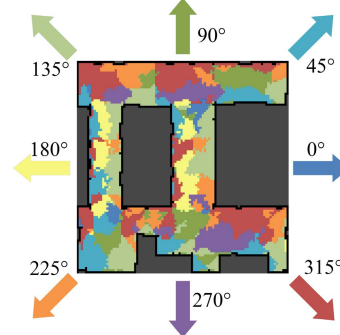
Fig. 3. Combining angles within a range of  $\phi$ .

Fig. 4. Orientations with maximum, LM for every position.

a)  $\Theta_1 = 360^\circ$ : In this case  $M = 1$ ; therefore, only one LM graph needs to be calculated. Path planning algorithms may be simply applied over  $R_{pass}$  to solve for  $p'_s$ .

b)  $\Theta_1 < 360^\circ$ ,  $\phi$  is variable: Since  $\theta_l$  is decoupled from  $\theta_r$  when a vehicle moves, the equipped LRF can always be set to point toward the orientation with best localizability (i.e., with highest  $l'(\mathbf{p})$ ). Similarly, path planning algorithms may be simply applied over  $R_{pass}$  to solve for  $p'_s$ . Fig.4 demonstrates orientations with highest  $l'(\mathbf{p})$  for every position in an example environment where  $M = 8$  and  $\Theta_1 = 180^\circ$ .

c)  $\Theta_1 < 360^\circ$ ,  $\phi$  is invariable: Since  $\theta_l$  is dependent on  $\theta_r$  and cannot change freely when the vehicle moves, an extra orientational constraint should be posed while adding points

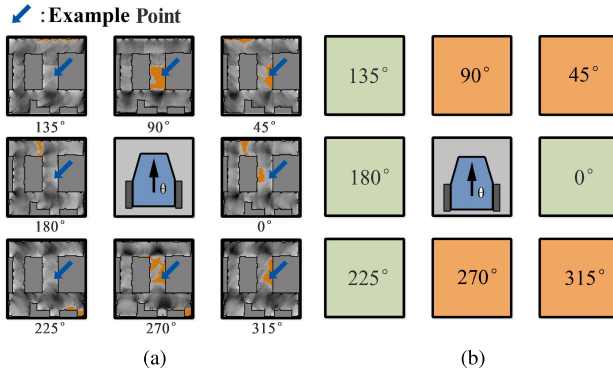


Fig. 5. Orientation constraints while path planning. (a) LM graphs and  $\mathbf{R}_{\text{pass}_m}$  under eight orientations. (b) Grids treated as obstacle (orange).

into paths. For example, if A\* algorithm is used for path planning, the constraint should be posed per moving directions between the current *expanding point* and adjacent *candidate points* to be added into open list. Fig.5 illustrates these directions and their corresponding constraints in an example environment ( $M = 8, \varphi = 0^\circ$ ). Suppose the current expanding point is situated at the example point marked with a blue arrow in Fig. 5(a). Since points located at  $45^\circ, 90^\circ, 270^\circ$  and  $315^\circ$  of the current expanding point are not within corresponding  $\mathbf{R}_{\text{pass}_m}$ , these points should be taken as obstacles and not be added into open list in the current iteration (see Fig. 5(b)).

4) If multiple candidate paths with equal shortest length exist, the final solution may be determined by the user based on other criteria or preferences, such as the time of generation of each path.

5) Extracting  $\mathbf{R}_{\text{pass}}$  of a new environment which includes step 1, 2 and 3 in Fig. 2 tend to be time consuming, therefore it is mostly computed offline; in real-time path planning, the pre-computed  $\mathbf{R}_{\text{pass}}$  is loaded into system before applying the desired path planning algorithm.

#### IV. SIMULATION AND DISCUSSION

##### A. Software Platform

Simulations were performed on a PC (Intel i5-3470 3.2Ghz CPU, 8GB RAM) using ROS open source platform. The related parameters in simulations are provided in Table II.

##### B. Simulation

An indoor office environment is used in the simulation, which includes two corridors and several rooms. One of the corridors passes by entrances to the rooms while the other one is located between two parallel walls. The PGM of the environment is first constructed using Gmapping SLAM (Fig. 6(a)). Since the LRF used in this simulation is omnidirectional ( $\Theta_1 = 360^\circ$ ),  $M = 1$  and (5) is used to calculate LM over the PGM. Fig. 6(b) shows the resulting LM graph, with obstacles colored in black. Normalization and binarization are then performed. As can be seen in Fig. 6(c), the discrete grids colored orange are of low LM. Followed by erosion and dilation operations, discrete grids are turned into connected regions, as demonstrated in Fig. 6(d). Parameter

TABLE II  
RELATED PARAMETERS

Parameter	Simulation	Indoor	Outdoor #1	Outdoor #2
$\Theta_1$	$360^\circ$	$180^\circ$	$180^\circ$	$180^\circ$
$D_1$	7 m	1 m	7 m	10 m
$R_l$	$1^\circ$	$1^\circ$	$1^\circ$	$1^\circ$
$N$	360	181	181	181
$M$	1	8	8	8
Map Width	24 m	12.45 m	113.4 m	20.8 m
Map Height	41 m	8.4 m	120 m	82 m
Grid Size	0.1 m	0.05 m	0.1 m	0.2 m
$\Delta x, \Delta y, \Delta \theta_l$	0.1 m,- $3 \times 3$ Cross	0.05 m, $1^\circ$ $3 \times 3$ Cross	0.1 m, $1^\circ$ $3 \times 3$ Cross	0.2 m, $1^\circ$ $3 \times 3$ Cross
$T_{\text{bin}}$	0.35	0.35	0.2	0.2
$T_{\text{incl}}$	200 pixels	800 pixels	500 pixels	200 pixels
$E_a$	-	-	0.1 m	-
$D_p$	-	-	7 m	10 m

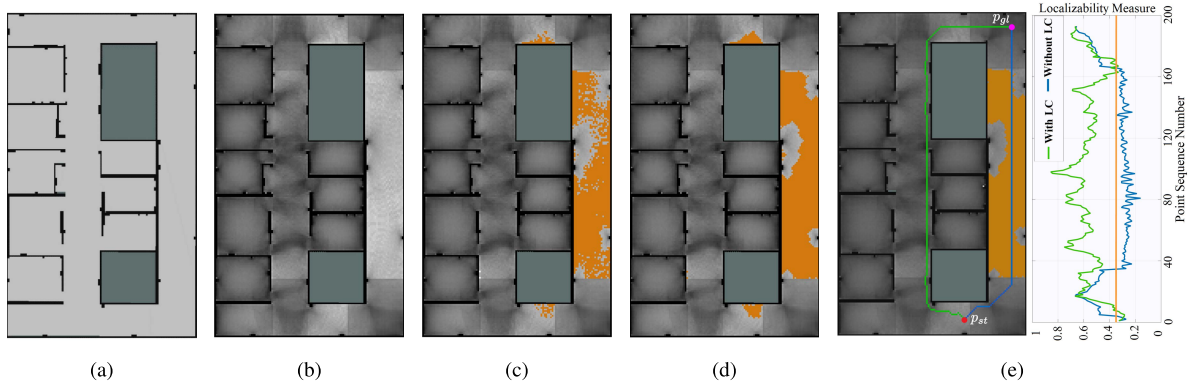
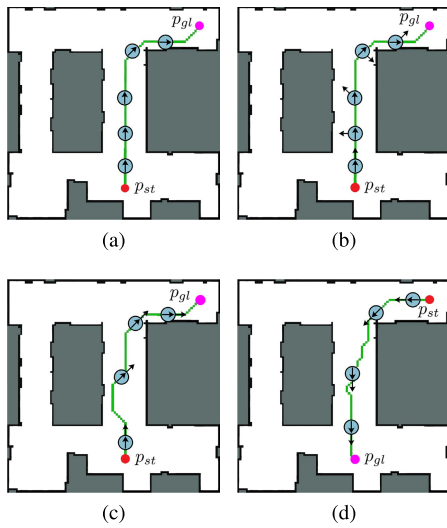
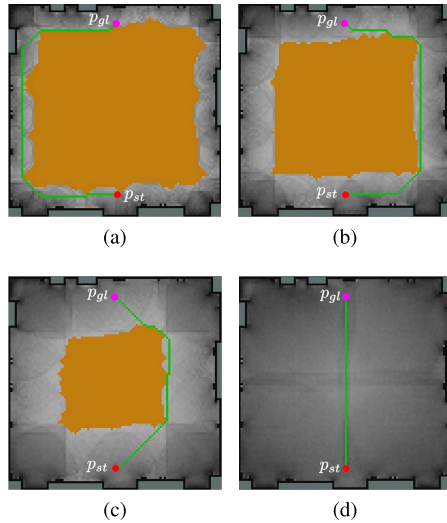
$T_{\text{incl}}$  is specified as 200 pixels, therefore those connected regions with an area smaller than 200 pixels are included into  $\mathbf{R}_{\text{pass}_1}$ .  $\mathbf{R}_{\text{pass}}$  is exactly the final processed  $\mathbf{R}_{\text{pass}_1}$ . The paths planned using A\* algorithm with LC (green) and without LC (blue) are shown in Fig. 6(e), with their LM along the path given at the right side (ranging from 0 to 1).  $T_{\text{bin}}$  is indicated by the orange constant line. As can be seen from the result, instead of taking the shorter path and going through the regions with low LM on the right side, the path generated by the proposed method chose to stay closer to featured structures and to traverse the corridor on the left side. Although the resulting path is longer in this case, compared to the path without LC, it promises better localizability throughout the path.

##### C. Discussion

1) *Influence of  $\Theta_1$  and  $\varphi$  on Resulting Paths:* Fig.7 shows four paths planned under different  $\Theta_1$  and  $\varphi$  in an indoor environment sized  $20 \text{ m} \times 20 \text{ m}$ . The blue circles, inner arrows and outer arrows represent the vehicle's position,  $\theta_r$  and  $\theta_l$  respectively. The start points are colored red, and the goal points are colored magenta.

Except in Fig.7(a) where  $\Theta_1 = 360^\circ$ , in the rest cases  $\Theta_1$  is set to  $180^\circ$ . In Fig.7(a), the vehicle observes rich environmental information at every position, therefore its configuration space is the entire map (leaving out obstacle grids). In this case the path is exactly the same as that of A\* without LC. In Fig.7(b), LRF may always point toward the orientation with maximum LM, thus it has the same configuration space and resulting path as in Fig.7(a). Extra orientational constraint is posed in Fig.7(c) and (d) because  $\varphi$  is not variable. Both the start and goal points are exchanged in Fig.7(d), resulting in a different path as in Fig.7(c). A simple conclusion is that the paths of those models with invariable  $\varphi$  are potentially longer due to a smaller configuration space.

2) *Influence of  $D_1$  on Resulting Paths:* The four sub-figures in Fig.8 all have  $\Theta_1 = 360^\circ$ , and have  $D_1$  increased according to display order. The environment is also

Fig. 6. Passable region extraction in simulation and comparison of result paths ( $\Theta_l = 360^\circ$ ,  $M = 1$ ).Fig. 7. Influence of  $\Theta_l$  and  $\varphi$  on paths. (a)  $\Theta_l = 360^\circ$ . (b)  $\varphi$  is variable. (c)  $\varphi$  is invariable (1). (d)  $\varphi$  is invariable (2).Fig. 8. Influence of  $D_l$  on paths. (a)  $D_l = 2$  m. (b)  $D_l = 3$  m. (c)  $D_l = 5$  m. (d)  $D_l = 10$  m.

sized  $20 \text{ m} \times 20 \text{ m}$ . When the vehicle is situated in such a spacious environment with comparatively short  $D_l$ , it cannot observe valid environmental information in the center part

of the map. This creates low LM regions (orange parts) in Fig.8(a) to (c), and causes the vehicle to move along walls with rich features. This result is in accordance with a similar conclusion stated in [24]. The area of low LM regions decreases as  $D_l$  increases, finally reaching zero, as in Fig.8(d). In this case, its configuration space is the entire map and again its path is also identical to that of A\* without LC. We see that in this set-up, the length of paths decreases as  $D_l$  increases.

## V. EXPERIMENTS

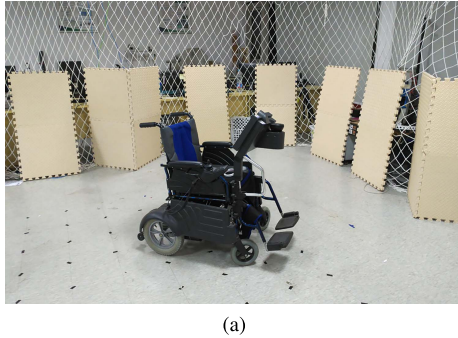
In this section, we first introduce the experimental platform that is used in both indoor and outdoor experiments. After that, planning results in an indoor environment, an outdoor environment with texture-poor regions and an outdoor environment with similarly-featured regions are demonstrated. In outdoor experiment #2, we compare the results of the proposed method with the method described in [24]. This is because [24] was the fundamental work that revealed the essence of other entropy-based methods such as [41] and is most comparable with the proposed method, in which the authors quantified the information content of the environment with the help of entropy before incorporating it into path planning. In all situations, A\* algorithm is adopted to solve for the shortest path  $p'_s$ .

### A. Experimental Platform

Intelligent wheelchair [42], [43] is one kind of autonomous vehicle which provides services for the elderly or disabled people by assisting them in moving around in both indoor and outdoor environments. In this paper, all experiments were carried out on a “JiaoLong” intelligent wheelchair (Fig.9). It is equipped with an encoder-based odometer, an LRF (SICK LSM111), a monitor (for data and related information display) and adopts DC motors with two-wheeled differential driving controlled by a Digital Signal Processor (DSP) motion controller. Programs and algorithms were executed on an industrial personal computer (IPC, Intel Core Duo T2500 2.0Ghz CPU, DDR2C667 3GB RAM). The particle filter-based localization algorithm used in the experiments was developed based on the source code of CARMEN toolkit [44], which draws random sampling particles around the current pose of the wheelchair, calculates a weight for each of the



Fig. 9. “JiaoLong” intelligent wheelchair.



(a)

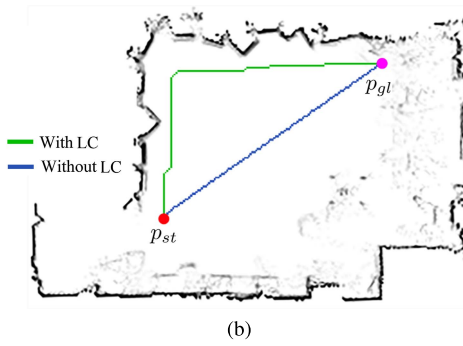


Fig. 10. (a) Indoor environment. (b) Planned paths in the indoor environment.

particles and finally outputs the estimated optimal pose in every step or iteration.

### B. Indoor Experiment

In this experiment, we compared the localization errors between the paths with and without LC. The indoor environment is shown in Fig.10(a). Foam boards were placed into the environment on one side to form rich-featured areas, and the center part remained empty. Throughout the experiment, real-time ground truth data was captured using Vicon Motion Capture System and sent to the wheelchair for display and recording. The localization error is defined as the Euclidean distance (always positive) between ground truth and the estimated position. The wheelchair was driven by a human to track the planned paths. Marks along the paths were made on the ground to help tracking. During navigation, the wheelchair is aligned to these marks using three point lasers that are attached to the wheelchair. Due to space limitation, in this experiment  $D_l$  is particularly set to a comparatively short

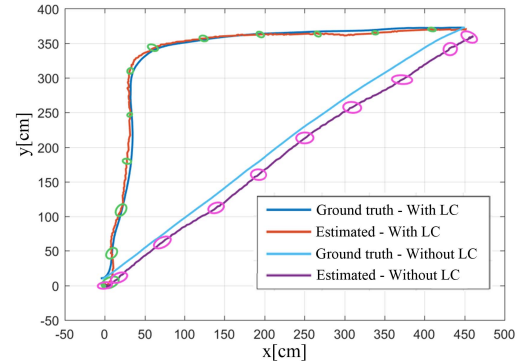


Fig. 11. Comparison of paths of experiment No.1.

TABLE III  
INDOOR LOCALIZATION ERRORS [cm]

Exp. No.	Without LC		With LC	
	Mean	S.D.	Mean	S.D.
1	14.4	3.6	4.1	1.9
2	15.5	3.3	4.7	2.1
3	15.4	3.9	5.2	1.7
4	14.8	3.8	5.2	3.6
5	15.9	4.1	5.0	2.0

range (1 m) to show the effectiveness of the proposed method. Other experimental parameters are listed in Table II.

As in the simulation, the PGM of the environment is first constructed using Gmapping SLAM method. After extracting  $\mathbf{R}_{\text{pass}}$  and performing path planning, the two resulting paths are generated (Fig.10(b)). Five sets of experiment are conducted, the resulting paths of experiment No.1 are shown in Fig.11. The localization covariance error ellipses (green and magenta) are drawn along the paths in Fig.11. As can be seen intuitively, the path with LC is much closer to its ground truth, while that without LC has a tendency to diverge as the wheelchair moves toward the goal point. By examining Table III, which shows the localization error along the paths, we see that in all five experiments, the average errors of paths with LC are about one third of those of paths without LC. This implies that along the proposed path, the wheelchair has a better pose tracking performance compared to the path without LC.

### C. Outdoor Experiment #1

To further investigate the localization performance along paths with and without LC, experiments were conducted near the eastern gate of Shanghai Jiao Tong University. The environment’s satellite image and PGM are given in Fig.12. Within the gate is a comparatively spacious square with four flower beds situated in the middle, and outside of the gate are two pathways leading to the left and to the right. Due to the lack of ground truth in this scenario, localization errors are measured and compared under autonomous navigation and human-driven navigation.

The existence of the four flower beds marked out in Fig.12(a) helps to improve wheelchair’s localization

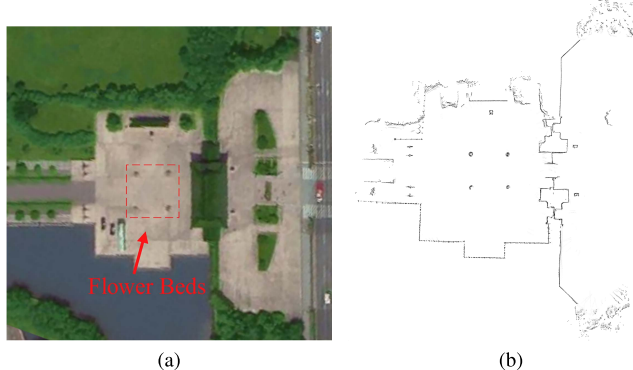


Fig. 12. Satellite map and PGM of outdoor environment #1.

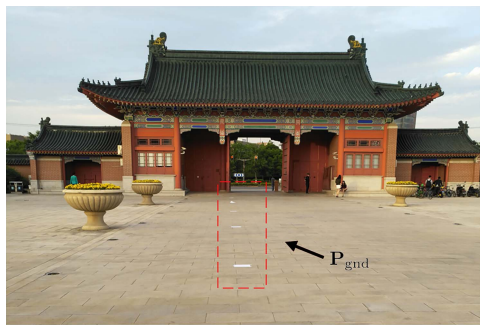


Fig. 13. Measuring poses marked on the ground.

performance in the middle part of the square. To demonstrate the difference between the paths with and without LC in a clearer vision, they were treated as dynamic obstacles and removed from the PGM when calculating LM and path planning. It is worth mentioning that this does not affect the localization accuracy of the adopted localization algorithm. By doing so, a texture-poor region in the middle of the square is formed. The LM graphs are provided in Fig.14, one example of planning result is shown in Fig.15.

The measuring points in PGM (including the goal point), noted as  $\mathbf{P}_{\text{map}} = \{p_{\text{map},1}, \dots, p_{\text{map},K}\}$ , are places where measurements of localization error are taken under autonomous navigation. They are selected along the path, starting from the start point with an equal distance  $D_p$  set between two adjacent ones.  $\mathbf{P}_{\text{gnd}} = \{p_{\text{gnd},1}, \dots, p_{\text{gnd},K}\}$  are measuring poses that consist of positions of  $\mathbf{P}_{\text{map}}$  and corresponding orientations while reaching  $\mathbf{P}_{\text{map}}$ , they are marked on the ground and used in measurements under human-driven navigation (Fig.13). To mark  $\mathbf{P}_{\text{gnd}}$ , poses (positions and corresponding orientations while reaching) of  $\mathbf{P}_{\text{map}}$  are first obtained through calculation. Subsequently, the wheelchair is located in the environment based on the original PGM (Fig.12(b)). When the poses of the wheelchair are matched with the obtained poses, those of the wheelchair are precisely marked on the ground with the help of three point lasers attached to the wheelchair and thereby  $\mathbf{P}_{\text{gnd}}$  are produced. Extra marks are also made to map the planned paths on the ground for human-driven navigation. After these preparations, the following experiments are performed:

1) *Autonomous Navigation*: In this case, the planned paths are autonomously tracked by the wheelchair according to the PGM. When the wheelchair arrives at a measuring

TABLE IV  
OUTDOOR LOCALIZATION ERRORS #1 [cm]

Mode Method	Autonomous				Human-driven			
	Without LC		With LC		Without LC		With LC	
Point No.	Mean	S.D.	Mean	S.D.	Mean	S.D.	Mean	S.D.
1	26.1	7.6	10.6	3.3	22.0	6.6	5.7	1.5
2	53.7	18.8	14.4	2.0	24.6	8.8	7.9	1.4
3	61.1	16.8	6.7	2.2	35.3	7.5	6.5	1.5
4	53.1	17.3	11.7	1.8	68.4	30.8	6.7	2.2
5	83.4	31.3	11.5	2.3	102.6	63.9	3.9	1.6
6	120.5	31.4	23.4	2.5	40.0	32.4	13.9	2.5
7	27.6	20.3	15.2	3.3	20.3	8.3	8.0	1.4
8	23.7	26.1	12.6	2.9	12.1	2.0	3.4	1.5
9	46.3	26.9	9.2	1.6	20.6	7.1	6.9	2.0
10	56.2	23.3	9.7	1.8	31.0	7.3	7.2	1.6
11	108.4	57.4	12.4	1.5	41.0	11.0	5.8	1.4
12	118.8	31.9	6.2	2.5	66.4	22.9	5.3	1.4
13	145.4	43.3	11.2	2.7	99.4	44.7	3.4	1.5
14	132.6	48.1	17.8	3.7	103.3	36.4	13.4	2.1
15	-	-	5.7	2.6	-	-	5.9	1.9
16	-	-	12.0	2.9	-	-	5.7	2.0
17	-	-	18.0	3.3	-	-	14.9	1.7
18	-	-	24.5	3.3	-	-	22.8	1.3

point  $p_{\text{map},k}$  with error allowance  $E_a$ , a stop is made and the ground distance (localization error) between its position and the corresponding  $p_{\text{gnd},k}$  is measured before it moves toward the next measuring point  $p_{\text{map},k+1}$ . During navigation, if the wheelchair reaches all  $\mathbf{P}_{\text{map}}$  in proper order within a reasonable time, we consider it a success, otherwise it is a failure.

This experiment was performed ten times for both of the paths respectively. For the path with LC, the wheelchair succeeded in all trials; for the path without LC, seven trials were successful, and three trials failed. The failures were mainly due to moving toward obstacles, which kept the wheelchair from following its path and reaching the next measuring point.

Localization error comparison was only made between successful trials of the two paths. According to Table IV, the errors of a path with LC is basically much less than that of a path without LC. More specifically, the errors of path with LC are more concentrated and are all within 30 cm. Comparatively large errors occurred at point No.6 (23.4 cm) and No.18 (24.5 cm), which is particularly due to the existence of bushes within the scan range of LRF. The errors of path without LC are spread over a wider range and exceed 100 cm (even up to 150 cm in some cases) at many points.

2) *Human-Driven Navigation*: In this case, the wheelchair is driven by a human to track the marks of planned paths on the ground. When it arrives at a measuring pose  $p_{\text{gnd},k}$ , a stop is made and the distance (localization error) between the position read from the wheelchair and the corresponding  $p_{\text{map},k}$  is calculated before it is driven toward the next measuring pose  $p_{\text{gnd},k+1}$ . During navigation, if the wheelchair reaches all  $\mathbf{P}_{\text{gnd}}$  without colliding with any obstacle in the PGM, we consider it as a success, otherwise as a failure. Note that in this case, since the localization errors are calculated while the wheelchair is accurately aligned to  $\mathbf{P}_{\text{gnd}}$ , smaller errors may be expected as compared to those in the previous experiment.

This experiment was performed ten times for both of the paths respectively. For the path with LC, once more, the wheelchair succeeded in all trials; for the path without LC, eight

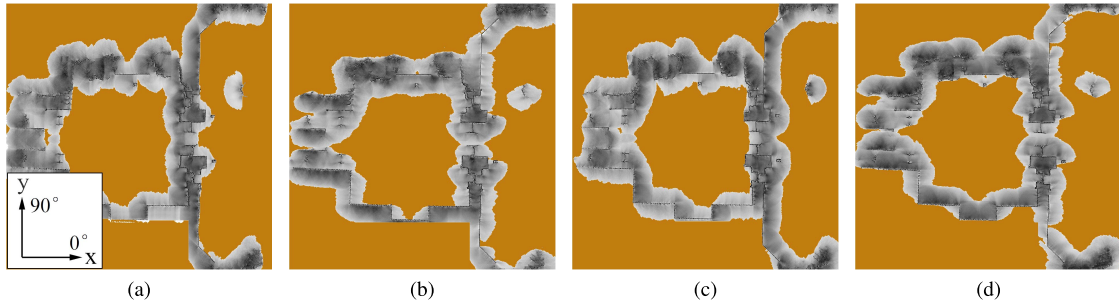
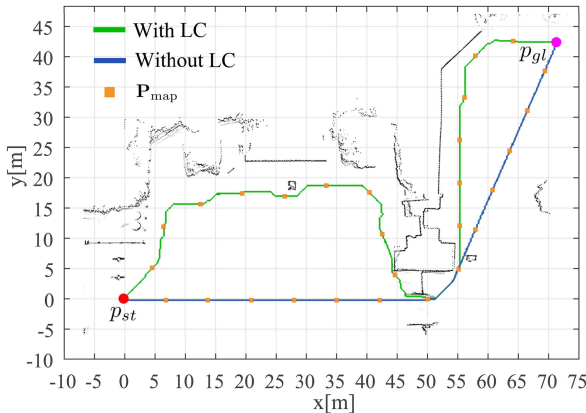
Fig. 14. LM graphs of outdoor environment #1. (a)  $\theta_l = 0^\circ$ . (b)  $\theta_l = 90^\circ$ . (c)  $\theta_l = 180^\circ$ . (d)  $\theta_l = 270^\circ$ .

Fig. 15. Planned paths in the outdoor environment #1.

trials were successful, and two trials failed. The failures were due to lack of valid LRF readings which causes the wheelchair to track its pose only relying on odometer. As the wheelchair navigates, the increasing accumulated localization error finally incurred these failures.

As in the previous experiment, the localization error comparison was only made between successful trials. According to Table IV, generally the localization errors of both paths decreased when compared to those in autonomous navigation. Once again, it is observable that errors of paths with LC are much less than those of paths without LC, and are mostly within 20 cm; similarly, the errors of paths without LC are comparatively large, with many exceeding 100 cm.

As can be seen from the results of the above two experiments, in both cases, the wheelchair achieved better overall localization performance and showed higher robustness when following paths with LC.

#### D. Outdoor Experiment #2

Another outdoor experiment is carried out to verify the feasibility of the proposed method in environments with similarly-featured regions. The experiment is performed on a road with greenbelts and walkways present on its both sides (see Fig.16). The trunks of the trees on the walkways are expected to provide sufficient information for the wheelchair to localize itself. The localization errors along the paths are measured under human-driven navigation as explained in outdoor experiment 1. An example of planning result of paths

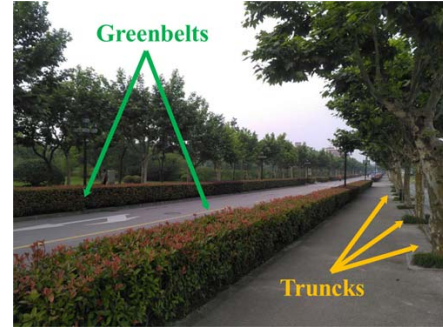
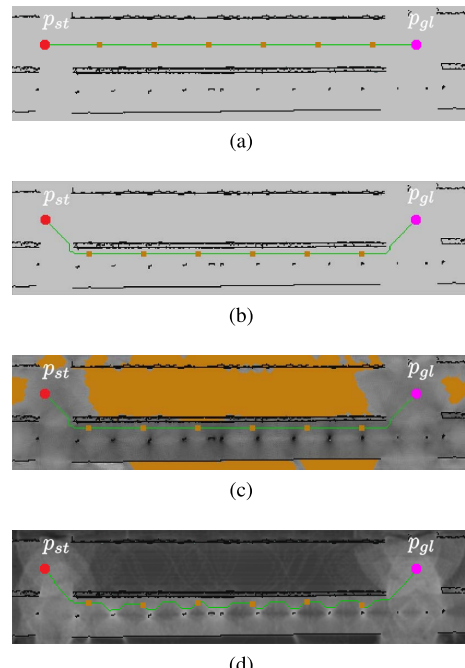


Fig. 16. Outdoor environment #2 with greenbelts and walkways on its both sides.

Fig. 17. Comparison of planning results. (a) Without LC. (b) With LC,  $\Theta_l = 180^\circ$ . (c) With LC,  $\Theta_l = 360^\circ$ . (d) Entropy-based method.

without LC, with LC and entropy-based is shown in Fig.17. It can be noticed that in this scenario, the paths planned with LC using  $\Theta_l = 180^\circ$  and  $\Theta_l = 360^\circ$  are identical.

This experiment was performed five times for each of the paths respectively. The wheelchair reached the goal point

TABLE V  
OUTDOOR LOCALIZATION ERRORS #2 [cm]

Mode Method	Human-driven					
	Without LC		With LC		Entropy-Based	
Point No.	Mean	S.D.	Mean	S.D.	Mean	S.D.
1	7.0	2.0	3.2	2.6	3.4	1.8
2	13.1	2.1	1.3	1.2	2.8	0.4
3	22.0	6.6	1.7	0.6	1.5	0.4
4	36.3	7.1	1.2	1.8	2.2	1.7
5	46.6	10.7	3.2	1.1	3.3	0.8
6	14.3	1.4	3.4	1.3	3.5	1.9
7	2.2	1.1	2.1	1.6	2.3	1.3

successfully in all trials. According to Table V, the path without LC has the greatest mean errors and standard deviations, while the other two paths possess much smaller ones. More specifically, the errors of path without LC increased as the wheelchair navigated in the similarly-featured region caused by the greenbelts. As the wheelchair continued to move toward the goal point, its localization errors dropped as soon as it observed distinguishable features at the end of the road. For the paths with LC and based on entropy, we can easily realize that both paths avoided region between the greenbelts and stayed close to the trunks. According to Fig.17(d), while the path based on entropy has similar localization error as compared with that of the proposed path, it tends to twist according to the contour of the changes in the *map of entropy* [24], as in this method the entropy term is integrated along with the path length into the cost function. When considering the cost of sensors, another shortcoming of the entropy-based method is that it is only applicable to an omni-directional scanning system ( $\Theta_1 = 360^\circ$ ), whereas the proposed method is not limited to this specific kind of observation model.

## VI. CONCLUSION

In this paper, a localizability constraint-based path planning method for autonomous vehicles is introduced. The proposed method provides a framework for global path planning that uses the pre-constructed PGM of the environment, considers the LRF sensor model, and solves for the shortest possible paths with localizability constraint specifically taken into account. Our method is not limited to any specific path planning algorithm in the optimization stage and can be easily realized by incorporating the LC into conventional path planning algorithms. In the simulation section, the method, which exhibited its applicability for LRF sensors of different models, is implemented and discussions on result paths are given. Through conducting real world experiments in both indoor and outdoor environments, along with simulation results, we have shown that in situations where there are low LM regions present in the environment, the path planned via the proposed method provides richer environmental information, effectively reduces the localization errors, and ensures better localization performance and higher robustness as compared to those planned without LC by avoiding these regions. The resulting paths of the proposed method demonstrated a tendency to stay close to rich-featured areas, which concurs with our intuitive expectation.

## REFERENCES

- [1] T. Cao, Z.-Y. Xiang, and J.-L. Liu, "Perception in disparity: An efficient navigation framework for autonomous vehicles with stereo cameras," *IEEE Trans. Intell. Transp. Syst.*, vol. 16, no. 5, pp. 2935–2948, Oct. 2015.
- [2] H. Zhu, K.-V. Yuen, L. Mihaylova, and H. Leung, "Overview of environment perception for intelligent vehicles," *IEEE Trans. Intell. Transp. Syst.*, vol. 18, no. 10, pp. 2584–2601, Oct. 2017.
- [3] R. Danescu, F. Oniga, and S. Nedevschi, "Modeling and tracking the driving environment with a particle-based occupancy grid," *IEEE Trans. Intell. Transp. Syst.*, vol. 12, no. 4, pp. 1331–1342, Dec. 2012.
- [4] J. Nilsson, J. Fredriksson, and A. C. E. Ödblom, "Reliable vehicle pose estimation using vision and a single-track model," *IEEE Trans. Intell. Transp. Syst.*, vol. 15, no. 6, pp. 2630–2643, Oct. 2014.
- [5] S. Yoon, S.-E. Yoon, U. Lee, and D. H. Shim, "Recursive path planning using reduced states for car-like vehicles on grid maps," *IEEE Trans. Intell. Transp. Syst.*, vol. 16, no. 5, pp. 2797–2813, Oct. 2015.
- [6] J. D. Hernández, E. Vidal, G. Vallicrosa, E. Galceran, and M. Carreras, "Online path planning for autonomous underwater vehicles in unknown environments," in *Proc. IEEE Int. Conf. Robot. Automat.*, May 2015, pp. 1152–1157.
- [7] S. C. Peters and K. Iagnemma, "Mobile robot path tracking of aggressive maneuvers on sloped terrain," in *Proc. IEEE/RSJ Int. Conf. Intell. Robots Syst.*, Sep. 2008, pp. 242–247.
- [8] Z. Sun, Q. Chen, Y. Nie, D. Liu, and H. He, "Ribbon model based path tracking method for autonomous land vehicle," in *Proc. IEEE/RSJ Int. Conf. Intell. Robots Syst.*, Oct. 2012, pp. 1220–1226.
- [9] L. Wei, C. Cappelle, and Y. Ruichek, "Unscented information filter based multi-sensor data fusion using stereo camera, laser range finder and GPS receiver for vehicle localization," in *Proc. 14th Int. IEEE Conf. Intell. Transp. Syst.*, Oct. 2011, pp. 1923–1928.
- [10] L. Wei, C. Cappelle, and Y. Ruichek, "Camera/laser/GPS fusion method for vehicle position under extended NIS-based sensor validation," *IEEE Trans. Instrum. Meas.*, vol. 62, no. 11, pp. 3110–3122, Nov. 2013.
- [11] S. Se, D. Lowe, and J. Little, "Local and global localization for mobile robots using visual landmarks," in *Proc. IEEE/RSJ Int. Conf. Intell. Robots Syst.*, vol. 1, Oct./Nov. 2001, pp. 414–420.
- [12] A. C. Murtra, J. M. M. Tur, and A. Sanfeliu, "Action evaluation for mobile robot global localization in cooperative environments," *Robot. Autom. Syst.*, vol. 56, no. 10, pp. 807–818, 2008.
- [13] A. R. Cassandra, L. P. Kaelbling, and M. L. Littman, "Acting optimally in partially observable stochastic domains," in *Proc. Nat. Conf. Artif. Intell.*, vol. 2, 1994, pp. 1023–1028.
- [14] L. P. Kaelbling, M. L. Littman, and A. R. Cassandra, "Planning and acting in partially observable stochastic domains," *Artif. Intell.*, vol. 101, nos. 1–2, pp. 99–134, 1998.
- [15] S. Candido and S. Hutchinson, "Minimum uncertainty robot path planning using a POMDP approach," in *Proc. IEEE/RSJ Int. Conf. Intell. Robots Syst.*, Oct. 2010, pp. 1408–1413.
- [16] S. Prentice and N. Roy, "The belief roadmap: Efficient planning in belief space by factoring the covariance," *Int. J. Robot. Res.*, vol. 28, nos. 11–12, pp. 1448–1465, Jul. 2009.
- [17] L. E. Kavraki, P. Svestka, J.-C. Latombe, and M. H. Overmars, "Probabilistic roadmaps for path planning in high-dimensional configuration spaces," *IEEE Trans. Robot. Automat.*, vol. 12, no. 4, pp. 566–580, Aug. 1996.
- [18] S. Chakravorty and S. Kumar, "Generalized sampling-based motion planners," *IEEE Trans. Syst., Man, Cybern. B, Cybern.*, vol. 41, no. 3, pp. 855–866, Jun. 2011.
- [19] S. M. LaValle and J. J. Kuffner, Jr., "Randomized kinodynamic planning," *Int. J. Robot. Res.*, vol. 20, no. 5, pp. 378–400, 2001.
- [20] F. Zhang, B. Grocholsky, and V. Kumar, "Formations for localization of robot networks," in *Proc. IEEE Int. Conf. Robot. Automat.*, vol. 4, Apr./May 2004, pp. 3369–3374.
- [21] D. Fox, "Markov localization—A probabilistic framework for mobile robot localization and navigation," Ph.D. dissertation, Dept. Comput. Sci., Univ. Bonn, Bonn, Germany, 1998.
- [22] S. D. Bopardikar, B. Englot, and A. Speranzon, "Multiobjective path planning: Localization constraints and collision probability," *IEEE Trans. Robot.*, vol. 31, no. 3, pp. 562–577, Jun. 2015.
- [23] Q. Li, W. Chen, and J. Wang, "Dynamic shared control for human-wheelchair cooperation," in *Proc. IEEE Int. Conf. Robot. Automat.*, May 2011, pp. 4278–4283.
- [24] N. Roy, W. Burgard, D. Fox, and S. Thrun, "Coastal navigation-mobile robot navigation with uncertainty in dynamic environments," in *Proc. IEEE Int. Conf. Robot. Automat.*, vol. 1, May 1999, pp. 35–40.

- [25] F. Celeste, F. Dambreville, and J.-P. L. Cadre, "Optimal path planning using cross-entropy method," in *Proc. 9th Int. Conf. Inf. Fusion*, Jul. 2006, pp. 1–8.
- [26] A. Censi, "On achievable accuracy for range-finder localization," in *Proc. IEEE Int. Conf. Rob. Autom.*, Apr. 2007, pp. 4170–4175.
- [27] A. Censi, "On achievable accuracy for pose tracking," in *Proc. IEEE Int. Conf. Robot. Automat.*, May 2009, pp. 1–7.
- [28] A. Ruiz-Mayor, J.-C. Crespo, and G. Trivino, "Perceptual ambiguity maps for robot localizability with range perception," *Expert Syst. Appl.*, vol. 85, pp. 33–45, Nov. 2017.
- [29] A. Díosí and L. Kleeman, "Uncertainty of line segments extracted from static SICK PLS laser scans," in *Proc. Austral. Conf. Robot. Automat.*, 2003.
- [30] E. Galceran, S. Nagappa, M. Carreras, P. Ridao, and A. Palomer, "Uncertainty-driven survey path planning for bathymetric mapping," in *Proc. IEEE/RSJ Int. Conf. Intell. Robots Syst.*, Nov. 2013, pp. 6006–6012.
- [31] B. Englot, T. Shan, S. D. Bopardikar, and A. Speranzon, "Sampling-based min-max uncertainty path planning," in *Proc. IEEE 55th Conf. Decis. Control*, Dec. 2016, pp. 6863–6870.
- [32] L. Fernández-León, J. Neira, and J. A. Castellanos, "Path planning in graph SLAM using expected uncertainty," in *Proc. IEEE/RSJ Int. Conf. Intell. Robots Syst.*, Oct. 2016, pp. 4594–4601.
- [33] Z. Liu, W. Chen, Y. Wang, and J. Wang, "Localizability estimation for mobile robots based on probabilistic grid map and its applications to localization," in *Proc. IEEE Int. Conf. Multisensor Fusion Integr. Intell. Syst.*, Sep. 2012, pp. 46–51.
- [34] B. Bobrovsky and M. Zakai, "A lower bound on the estimation error for Markov processes," *IEEE Trans. Autom. Control*, vol. AC-20, no. 6, pp. 785–788, Dec. 1975.
- [35] Y. Wang, W. Chen, and J. Wang, "Map-based localization for mobile robots in high-occluded and dynamic environments," *Ind. Robot, Int. J.*, vol. 41, no. 3, pp. 241–252, 2014.
- [36] Y. Wang, W. Chen, J. Wang, and H. Wang, "Active global localization based on localizability for mobile robots," *Robotica*, vol. 33, no. 8, pp. 1609–1627, 2015.
- [37] Y. Bar-Shalom, X. R. Li, and T. Kirubarajan, *Estimation With Applications to Tracking and Navigation: Theory Algorithms and Software*, vol. 53, no. 6. Hoboken, NJ, USA: Wiley, 2001.
- [38] A. Censi, "An accurate closed-form estimate of ICP's covariance," in *Proc. IEEE Int. Conf. Robot. Automat.*, Apr. 2007, pp. 3167–3172.
- [39] G. Grisetti, C. Stachniss, and W. Burgard, "Improved techniques for grid mapping with Rao-Blackwellized particle filters," *IEEE Trans. Robot.*, vol. 23, no. 1, pp. 34–46, Feb. 2007.
- [40] P. E. Hart, N. J. Nilsson, and B. Raphael, "A formal basis for the heuristic determination of minimum cost paths," *IEEE Trans. Syst. Sci. Cybern.*, vol. SSC-4, no. 2, pp. 100–107, Jul. 1968.
- [41] S. Candido and S. Hutchinson, "Minimum uncertainty robot navigation using information-guided POMDP planning," in *Proc. IEEE Int. Conf. Robot. Automat.*, May 2011, pp. 6102–6108.
- [42] S. P. Parikh, V. Grassi, Jr., V. Kumar, and J. Okamoto, Jr., "Integrating human inputs with autonomous behaviors on an intelligent wheelchair platform," *IEEE Intell. Syst.*, vol. 22, no. 2, pp. 33–41, Mar. 2007.
- [43] B. M. Faria, L. P. Reis, N. Lau, A. P. Moreira, M. Petry, and L. M. Ferreira, "Intelligent wheelchair driving: Bridging the gap between virtual and real intelligent wheelchairs," in *Progress in Artificial Intelligence* (Lecture Notes in Computer Science), 2015, pp. 445–456.
- [44] R. Simmons *et al.*, "GRACE: An autonomous robot for the AAAI robot challenge," *AI Mag.*, vol. 24, no. 2, pp. 51–72, 2003.



**Behnam Irani** received the B.S. degree in automation and the M.S. degree in control science and engineering from Shanghai Jiao Tong University (SJTU), Shanghai, China, in 2015 and 2018, respectively.

From 2015 to 2018, he was with the Autonomous Robot Laboratory, SJTU. His research interests include localization, path planning, and navigation for mobile robots.



**Jingchuan Wang** received the B.Eng., M.Phil., and Ph.D. degrees in control theory and control engineering from Shanghai Jiao Tong University (SJTU), Shanghai, China, in 2002, 2005, and 2014, respectively, where from 2005 to 2015, he was an Assistant Professor. Since 2016, he has been an Associate Professor. His research interests include service robot and mobile robot localization and navigation.



**Weidong Chen** received the B.S. and M.S. degrees in control engineering and the Ph.D. degree in mechatronics from the Harbin Institute of Technology, Harbin, China, in 1990, 1993, and 1996, respectively. Since 1996, he has been at Shanghai Jiao Tong University, Shanghai, China, where he is currently the Deputy Dean of the Medical Robotics Institute and a Professor and the Chair of the Department of Automation. He is the Founding Director of the Autonomous Robot Laboratory, Shanghai Jiao Tong University. He was a Visiting Professor with the Artificial Intelligence Laboratory, University of Zurich, Switzerland, in 2012. He was a Visiting Professor with the Brain Science Life Support Research Center, University of Electro-Communications, Japan, from 2016 to 2019. He was recognized by the New Century Excellent Talents in the University of the Ministry of Education of China in 2007 and as a Shanghai Shuguang Scholar in 2004. His current research interests include autonomous robotics, assistive robotics, and medical robotics.